MNRAS 000, 1–15 (2023) Preprint 3 July 2023 Compiled using MNRAS LATEX style file v3.0

The Galactic Chemical Evolution of Carbon: Implications for Stellar Nucleosynthesis

Daniel A. Boyea,[1]★ A. N. Other,[2] Third Author[2,3] and Fourth Author[3]
[1]*Department of Astronomy, the Ohio State University, 191 W. Woodruff, Columbus, OH 43210, USA*

Accepted XXX. Received YYY; in original form ZZZ

ABSTRACT

Limited knowledge of stellar physics leads to uncertainties in elemental yield predictions. As an independent approach, we constrain the nucleosynthetic yields of C using multi-zone Galactic chemical evolution models. By matching the median trends of [C/Mg]-[Mg/H] and [C/Mg]-[Mg/Fe] in APOGEE subgiant stars, we find that high-mass and low-mass stars contribute ∼80% and ∼20% of total C production respectively. To match the normalization of the trends, we estimate the massive star C/Mg yield ratio $y^{cc}_{C}/y^{cc}_{Mg} = 1.57 + 0.59\,(Z/Z_{\odot})$, explaining the [C/Mg]-[Mg/H] trend when including the low mass C contribution. Variations in the star formation history only slightly impact the low [Mg/Fe] tail of the [C/Mg]-[Mg/Fe] relation. However, most of the scatter in the [C/Mg]-[Mg/H] distribution can be attributed to measurement errors and radial migration. Due to the degeneracy between the normalization of elemental yields and the strength of mass-loading in Galactic outflows, we am only able to constrain the relative yields of C/Mg and its metallicity dependence. While measurements of gas-phase C abundances are challenging, our model is broadly consistent with the [C/O]-[O/H] trend observed in compiled literature measurements.

1 INTRODUCTION

Carbon is a distinctive and well-studied element in astronomy. Formed in the cores of stars during He fusion, C is the lightest directly synthesized element after He, one of the only light elements formed in low-mass stars, and one the most abundant metals[1]. C structurally changes the environments it pollutes, modifying stellar evolution, facilitating the formation of stars and planets, and forming the basis of earthly life. As such, understanding the origin of C has wide ranging implications. While we know both lower-intermediate-mass and high-mass stars produce C, the relative importance of each process is still unknown.

Galactic chemical evolution is a powerful tool in understanding the origin of elements. Each enrichment process has distinct chemical signatures and timescales, enabling us to reconstruct chemical histories. Many previous works have used GCE in attemt to understand C abundances, whether through using theoretical stellar models (Dearborn et al. 1978; Prantzos et al. 2018; Chiappini et al. 2003) or understanding observation (Tinsley 1979; Henry et al. 2000; Bensby & Feltzing 2006; Rybizki et al. 2017; Berg et al. 2019; Kobayashi et al. 2020). (See also review in Romano 2022.) Every study agrees that C is produced by a combination of high-mass and lower-intermediate mass stars, different studies disagree on which process is dominant. For example CITES conclude high-mass stars dominate wherease CITES conclude lower-intermediate mass stars contribute the majority of C. C is also generally understood to have strong metalliicity dependent CCSNe enrichment.

One of the primary uncertainties of GCE models are nucleosynthetic yields. Yield predictions – the amounts of each chemical element stars produce – are shaped by poorly understood processes, including mass loss, nuclear reaction rates, rotational mixing, convection, and explodability (Romano et al. 2010; Karakas & Lattanzio 2014; Ventura et al. 2013; Limongi & Chieffi 2018; Griffith et al. 2021). To better understand where carbon comes from and how it evolves, our aim is to use a combination of recent high-resolution observations from APOGEE and multi-zone models to develop estimates of the required C yields to reproduce galactic trends. Johnson et al. (2023) examined similar GCE models of N (which is closely related to C), finding that trends in N and O are explained by the metallicity dependence of N/O yields. Here, we extend their models to C, deriving similar constraints on C/Mg yields. We assess which yield prescriptions reproduce Galactic abundance trends while investigating the impact of GCE model assumptions, such as SFH and outflow mass loading.

We know, from observations of MW stars and extragalactic gas measurments, that C/O traces a banana shape in O/H (see 12). At very low metallicities, C/O decreases with increasing metallicity, from observations of halo stars and damped Lyman-alpha systems[2] (Nissen et al. 2014; Cooke et al. 2017; Fabbian et al. 2009). However, the trend reverses around $[O/H] \approx -1$[3]. C/O instead increases with increasing metallicity in observations of HII regions and Milky Way stars (Berg et al. 2019; see discussion in section 5.6).

However, observations of C are not without challenges. As stars ascend the red giant branch (RGB) at the end of H core burning, C abundances are changed by *first dredge up*[4]. This has the benefit of allowing C/N to be used as an age indicator in RGB stars (Masseron & Gilmore 2015; Martig et al. 2016; Hasselquist et al. 2019; Vincenzo et al. 2021), but evolved stars are no longer as useful for determining birth abundances. Works such as Vincenzo et al. (2021) attempt to correct for these changes but this requires MESA stellar modeling.

[1] Astronomers are not chemists. By metallicity, we mean the (mass) fraction of any element which is not H or He, denoted by Z. For the sun, $Z_{\odot} = 0.014$.

[2] DLAs; high redshift clouds of gas observed as absorption lines in yet higher redshift quasars

[3] In this paper, we use the standard notation for chemical abundances. $[A/B] = \log_{10}(A/B) - \log_{10}(A_{\odot}/B_{\odot})$, i.e. $[A/B]$ is the logarithm of the ratio between A and B, scaled such that $[A/B] = 0$ for the sun. Solar abundances are as measured in Asplund et al. (2009).

© 2023 The Authors

In optical spectroscopy, C lines are relatively faint, and surveys such as GALAH struggle against low detection rates, potentially biasing sample measurments. While APOGEE includes more reliable C_2 lines, there is an additional risk of systematics because ..... In the gas phase, HII regions are our best window into C abundances in our galaxy and extragalactic regions including dwarf. Unfortunantly, C lacks strong optical emission lines. Approaches use either recombination lines or ... in the ultraviolet, but these methods disagree, making gas-phase abundances a limited metric for GCE models of C.

As our primary observational constraint, we use a sample of subgiant stars from the APOGEE (Majewski et al. 2017). selected by the criteria in Roberts et al. (2023, in prep; see Appendix A). According to stellar evolution theory and observations (Gilroy 1989; Korn et al. 2007; Lind et al. 2008; Souto et al. 2018, 2019), these stars have not yet experienced first dredge up (FDU) but have well-mixed envelopes. So, subgiant surface abundances should represent their birth composition. Fig. 1 shows the subgiant sample plotted in [C/Mg]-[Mg/H] and [C/Mg]-[Mg/Fe]. [C/Mg] increases with metallicity, and [C/Mg] decreases with [Mg/Fe] at fixed [Mg/H]. Using these trends, we will develop a model of the enrichment sources and evolution of C.

Johnson et al. (2023) compare their model against the Vincenzo et al. (2021) sample of APOGEE (Majewski et al. 2017) RGB stars. Vincenzo et al. (2021) use MESA stellar evolution models (Paxton et al. 2011) to correct for the effects of First Dredge Up (FDU). We instead use the Roberts et al. (2023, in prep.) sample of APOGEE subgiants. Subgiant stars have not undergone FDU but have well-mixed atmospheres, so their atmospheric C and N abundances are still reflective of their birth abundances and do not need mixing corrections. We only compare the models to the low-α sequence unless otherwise specified. The selection criteria and differences between the samples are described in more detail in Appendix A.

2 NUCLEOSYNTHESIS

Yields – the amounts of each chemical element stars synthesise – are central to studies of galactic chemical evolution (GCE). In this section, we discuss the yield choices of our model and literature models for C yields. We focus on three nucleosynthetic pathways: asymptotic giant branch (AGB) stars, core collapse supernovae (CCSNe), and type Ia supernovae (SNe Ia). C is produced in both AGB and CCSNe stars. We also use Mg and Fe as tracers of CCSNe and SNe Ia enrichment respectively. O and Mg are produced almost entirely from CCSNe with metallicity-independent yields, making each element. In contrast Fe is produced in similar amounts by CCSNe and SNe Ia.

After a single stellar population (SSP)[5] forms, CCSNe are the first chemical enrichers. CCSNe explode within $\lesssim 40$ Myr, providing light elements (C, O, and Mg) and heavier elements (Fe and beyond). Next, low-mass stars begin to reach the end of their lives. By shedding their outer layers, AGB stars are important sources of C, N, and neutron capture elements. Finally, white dwarfs explode in SNe Ia, releasing Fe and other iron-peak elements.

To quantify yields, we define the stellar yield to be the fraction of a stars initial mass which is newly synthesized and released as a given element. For an element X and star with mass M, the net-fractional stellar yield $\curlywedge$ is

$$\curlywedge_X = \frac{M_{\rm ejected}}{M_{\rm birth}} \Delta Z_X \tag{1}$$

where $M_{\rm ejected}$ and $M_{\rm birth}$ are the total ejected mass and the birth mass of the star, and ΔZ_X is the change in mass fraction of abundance X from birth to ejected. For example, if a $1\,M_\odot$ star has $\curlywedge_C = 10^{-3}$, then the star will add $10^{-3}\,M_\odot$ of new C to the interstellar medium. Although per-star yields are necessary to compute AGB star enrichment rates in GCE models, IMF-averaged yields are useful in interpreting their predictions. Given the fractional yield $\curlywedge(M, Z)$ as a function of initial stellar mass M and metallicity Z, the IMF-averaged yield is given by

$$y_X(Z,t) = \frac{\int_{M_{\rm min}(t)}^{M_{\rm max}} \curlywedge_X(M,Z) \frac{dN}{dM}\, M\, dM}{\int \frac{dN}{dM}\, M\, dM} \tag{2}$$

where dN/dM is the IMF, $M_{\rm max} = 100\,M_\odot$ is the maximum stellar mass, and $M_{\rm min}(t)$ is the mass of stars with lifetime t.[6] We use $t = 10$ Gyr for total yields when t is not used. To calculate the IMF-averaged net yields, we use the Versatile Integrator for Chemical Evolution code (VICE[7]).

We adapt the yield choices of elements besides C from Johnson et al. (2021, 2023). Table 1 contains our fiducial yields. Following Johnson et al. (2021, 2023), we also take the SNe Ia delay time distribution to be a $t^{-1.1}$ power-law, as suggested by the observations of Maoz et al. (2012).

Table 1. Yields for the fiducial model (in units of SSP birth mass). See Section 2.1 for the definition of C11.

Element	y_C^{cc}	$\curlywedge^{AGB}$	y^{SNeIa}
C	$0.0028 + 0.001\,(Z/Z_\odot)$	$2.9 \times$ C11	0
Mg	0.00185	0	0
Fe	0.0012	0	0.00214
N	0.00072	$9 \times 10^{-4}\,(Z/Z_\odot)\,M$	0

2.1 Asymptotic Giant Branch Stars

An AGB star is a low-mass star ($\lesssim 8 M_\odot$) during its final phase of evolution. In an AGB star, two competing processes determine the outcome of C production: *third dredge up* and *hot bottom burning*. Third dredge up accompanies thermal pulses in AGB stars, where material from the CO core is mixed with the envelope, increasing surface C abundances (Karakas & Lattanzio 2014). The C yields of the star are increased as this C-enhanced envelope is released to the interstellar medium. Hot bottom burning is the activation of the CNO cycle[8] at the bottom of the convective envelope when $T \gtrsim 50$ MK. Because the ^{14}N proton capture is the slowest component of the CNO cycle, the CNO cycle converts nearly all ^{12}C into ^{14}N (Adelberger et al. 2011).

Hot bottom burning and third dredge-up result in mass-dependent

[4] First dredge up (FDU) is when material from CNO processed core is mixed with the (convective) stellar envelop during the ascent onto the RGB. As a result, C is decreased and N is increased depending on the strength of this process and the envelop mass.

[5] SSP: Single stellar population. Technical name for a group of stars born in the same conditions at the same time, i.e. an open cluster.

[6] In our model, the mass-lifetime relation is $\log \tau_M = 1.02 - 3.57 \log M + 0.90\,(\log M)^2$, where τ_M is in Gyr, from Larson 1974

[7] VICE is available at https://github.com/giganano/VICE

[8] The CNO cycle is a series of proton-capture reactions with CNO elements resulting in energy generation and the creation of an α particle. $^{12}C(p,\gamma)^{13}N(\beta^+,\nu_e)^{13}C(p,\gamma)^{14}N(p,\gamma)^{15}O(\beta^+,\nu_e)^{15}N(p,\alpha)^{12}C$.

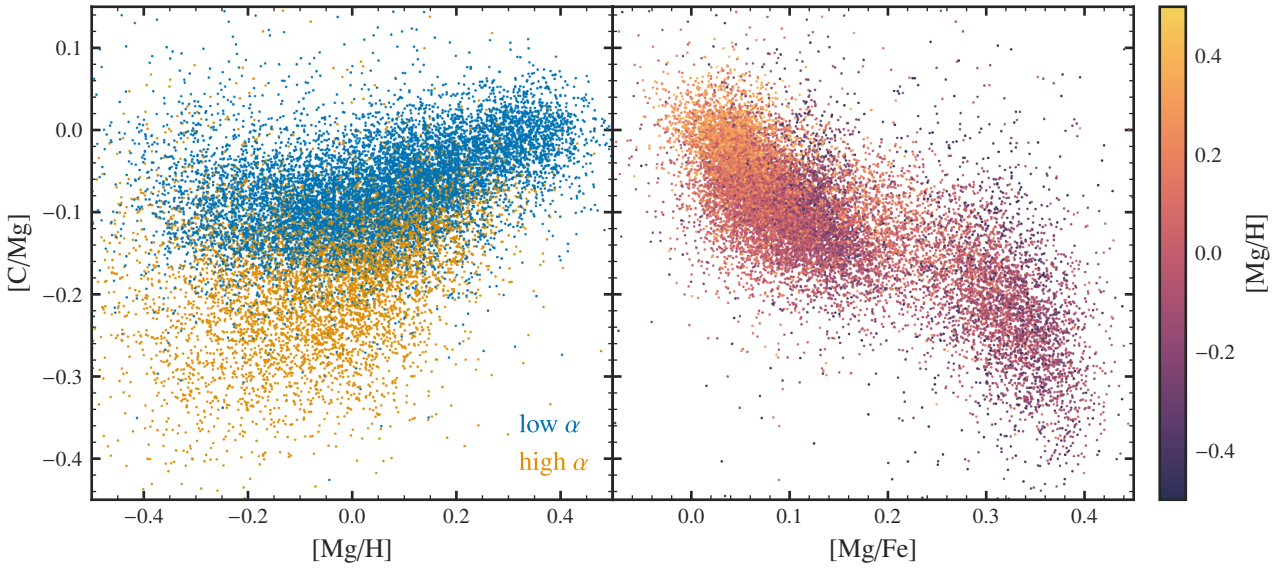

Figure 1. The [C/Mg] ratio against [Mg/H] (top) and [Mg/Fe] (bottom) for the Roberts et al. (2023, in prep.) sample of APOGEE subgiants. On the top, we plot high and low-α stars in blue and orange, using the separation defined in Equation A2 (the high and low-α stars are named for their high or low α-element to Fe ratios, or in this case, Mg/Fe). On the bottom, we colour-code stars according to their [Mg/H] abundance.

C yields. Stars less than about??2 $M_\odot$ do not experience third dredge-up. As a result, these stars C abundances are only affected by first dredge-up, resulting in little change to C yields or slight destruction of C. In 2?? to 4?? $M_\odot$ stars, third dredge up becomes important, enriching the outer layers with C, making these stars the most important producers of C. In massive, high-metallicity AGB stars, both hot bottom burning and third dredge up occur; however, third dredge up is much more efficient, resulting in significant ^{12}C destruction.

In this work, we explore four different sets of AGB star yield tables from literature, providing necessary well-sampled grids in mass and metallicity. We refer to the yields from the following studies as the following.

- `C11`: Cristallo et al. (2011, 2015)
- `K10`: Karakas (2010)
- `V13`: Ventura et al. (2013, 2014, 2018, 2020)
- `K16`: Karakas & Lugaro (2016); Karakas et al. (2018)

In Appendix B, the masses, metallicites, and notable differences between each yield set are briefly described. For our models to match observations, we find that need to uniformly amplify these yield tables. We use `C11` table, amplified by a factor of 2.9, as the fiducial AGB yield.

Fig. 2 compares the stellar AGB C yield for these four models. Note that the net yields may be negative if a star ejects material with a lower average C abundance than the material the star was formed from. Most models agree on the qualitative shape of the net fractional AGB C yield—stars with masses between about 2–4 $M_\odot$ have the highest fractional C yields. As metallicity increases, the total AGB C yield decreases and the mass of the peak increases.

Fig. 3, on the left, shows the total production of C by AGB stars in a SSP at an age t, i.e. $\Lambda_C(Z_\odot, t)$. As the mass range $2\,M_\odot \lesssim M \lesssim 4\,M_\odot$ is most important for C production, about half of C production occurs before ~1 Gyr, similar to SNe Ia Fe. `K10` and `K16` weight C production more heavily towards high-mass AGB stars resulting in a faster enrichment delay time, whereas the `C11` and `V13` models predict a slightly longer timescale of ~1 Gyr. In any case, little to no C is produced more than 2 Gyr after a star formation event. In contrast, Fe production continues steadily for 10 Gyr.

The right panel of Fig. 3 shows IMF-averaged C yields for each AGB model as a function of metallicity Z. `V13` differs in that it shows a non-monotonic metallicity dependence. However, this effect is only for models with $\log Z/Z_\odot \lesssim -1$. Otherwise, models differ only in their yield normalization and metallicity dependence. All models predict yields within a factor of ~2 for fixed metallicity. For example, the three models `C11`, `K10`, and `K16` predict y_C^{AGB} to be between 0.006 and 0.008 at solar metallicity, but `C11` has a much shallower metallicity dependence than the `K10` and `K16` models. `V13` instead predicts a yield ~0.004. As shown in the right panel of Fig. 3, with increasing Z, C enrichment occurs earlier, and C destruction in low-mass stars leads to a declining C abundance at late times.

2.2 Core Collapse Supernovae

Massive stars form ^{12}C in their cores through the triple–α process. However, only C ejected through supernovae and stellar winds contributes to the yield. While there are many stellar models providing predictions of CCSNe yields, the results of these models are highly uncertain due to the many stellar modeling uncertainties.

Fig. 4 plots calculations of the IMF-integrated yields, defined with Eq. 2 (computed using VICE's `vice.yields.ccsne.fractional` function). CCSNe models predict a wide range of C yields, spanning almost a factor of ten. Both the Nomoto et al. (2013) and Limongi & Chieffi (2018) models show positive metallicity dependence. The Limongi & Chieffi (2018) models also include rotation, showing that variations in the rotational velocity of the star can dramatically increase the magnitude and metallicity dependence of y_C^{cc}. Rotation induces more mixing allowing the CO core to grow larger. As we will later show, CCSNe C production needs to be strongly metallicity-

There are other less important minor branches of the CNO cycle (Adelberger et al. 2011).

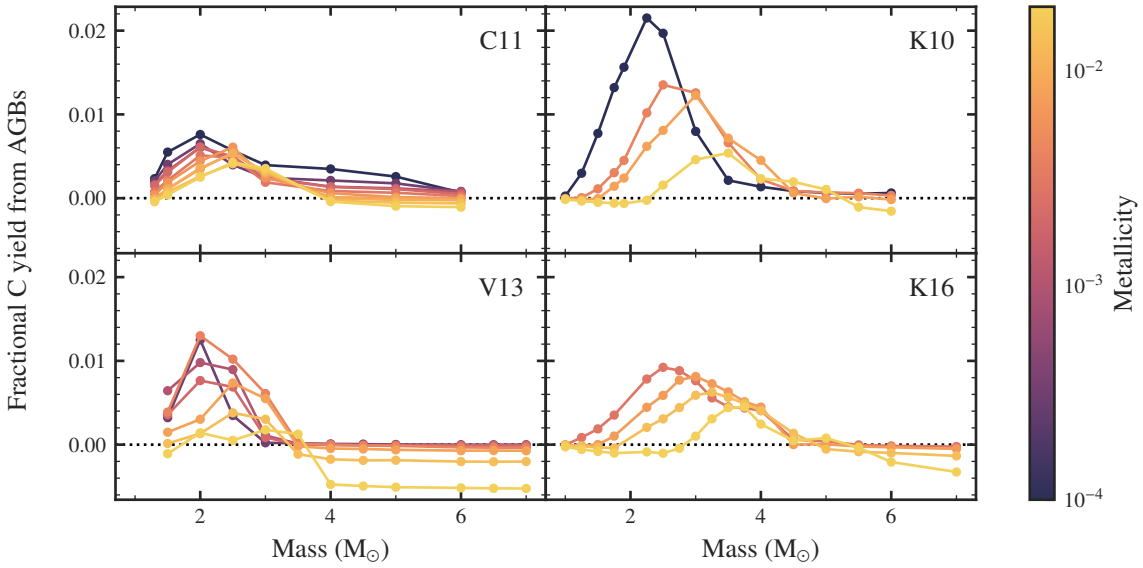

Figure 2. The net fractional AGB C yield plotted as a function of initial stellar mass M and colour-coded according to metallicity. The black dashed line shows $\hat{\kappa} = 0$ for reference. Each panel represents yields from one of four AGB models: `C11`, `K10`, `V13`, `K16` (see Section 2.1 and Appendix B).

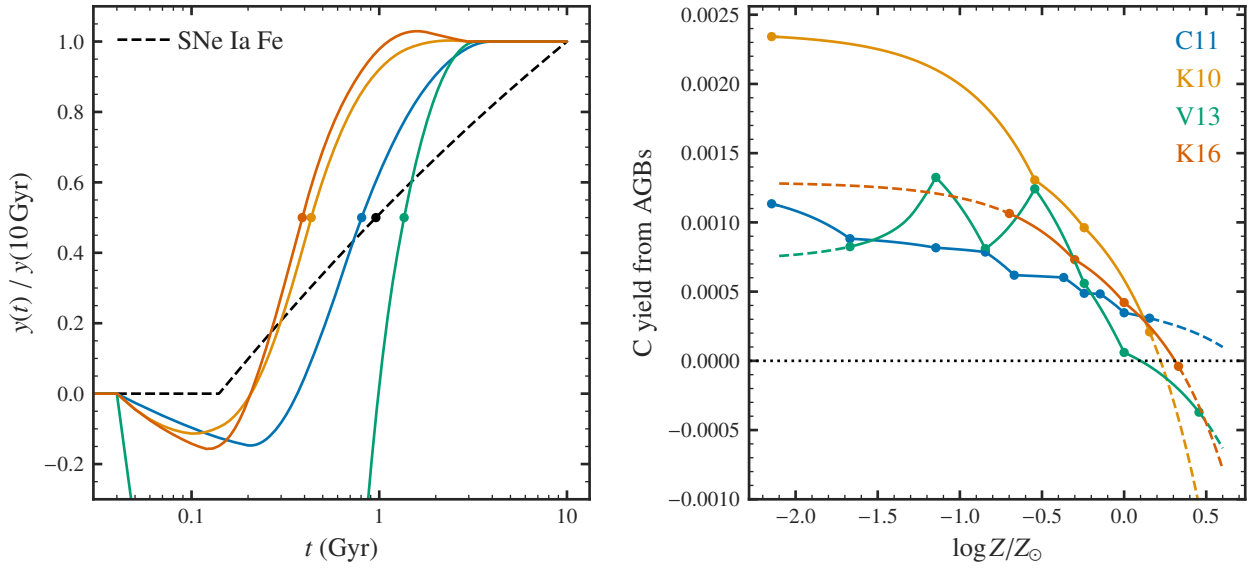

Figure 3. C production by AGB stars as a function of SSP age, normalized to the total mass $M_{\rm tot}$ produced at $t = 10$ Gyr. **Left:** The four AGB yield models from literature at solar metallicity (`C11`, `K10`, `V13`, or `K16`). The dashed black line shows the delay time distribution of type Ia supernovae ($\propto t^{-1.1}$) for comparison. **Right:** The (IMF-weighted) AGB C yield $y_{\rm C}^{\rm agb}$ as a function of metallicity for each of the AGB yield models. ($y_{\rm C}^{\rm agb}$ is the net mass of C produced by AGB stars per unit mass of star formation, after 10 Gyr and assuming a Kroupa 2001 IMF.)

dependent at $Z/Z_\odot \approx 1$, which is consistent with the Limongi & Chieffi (2018) rapidly rotating models.

Fig. 4 shows the `C11` AGB model for comparison on the left. Especially at $Z \approx Z_\odot$, most CCSNe models dominate AGB C production. Later, we will also show empirically this is the case. On the right of Fig. 4, we also show the CCSNe [C/Mg] ratio, defined by

$$[\mathrm{C/Mg}]^{\rm CC} = \log_{10}\left(\frac{y_{\rm C}^{\rm cc}}{y_{\rm Mg}^{\rm cc}}\right) - \log_{10}\left(\frac{Z_{\rm C,\,\odot}}{Z_{\rm Mg,\,\odot}}\right). \quad (3)$$

If only CCSNe produced C, then $[\mathrm{C/Mg}]^{\rm CC}$ describes the equilibrium abundance of [C/Mg]. Once again, different CCSNe models span a large range in [C/Mg]. we chose to instead parameterize $y_{\rm C}^{\rm cc}$ to enable agreement with observations, as most CCSNe models fail to achieve near-solar [C/Mg]. Assumptions about the explodability landscape affect C and Mg production. Increasing the fraction of stars that explode increases $y_{\rm C}^{\rm cc}$, as stars that directly collapse do not contribute to explosive yields (Griffith et al. 2021). However, C is relatively unaffected by the black-hole landscape, as very massive stars contribute C through enriched winds. Since Mg is formed deeper in the core of high-mass stars, the Mg yield drops much more steeply, so models where few stars explode (S16/W18) have higher [C/Mg].

CCSNe models do not reach [O/Mg] due to overproduction of O or underproduction of Mg, or both (Griffith et al. 2021). Here, we assume [O/Mg] = 0, which is not compatible with CCSNe models but is consistent with APOGEE observations (Weinberg et al. 2019, 2022).

Out model predictions of [C/Mg] and [C/H] are identical. There is a slight slope in [O/Mg] with metallicity, so this could add a systematic to our model.

As we focus on constraining relative yields, we neglect O and Mg yield variations in the main text (excluding the uniform scaling of yields and massloading in Section 5.5). There is substantial variation in predicted Mg yields. Most models predict relatively flat trends metallicity (even with rotation as in Limongi & Chieffi 2018). However, the variation is significant and our adopted $y^{\rm cc}_{\rm Mg}$ yield is much higher than most models. This is a known problem (see Griffith et al. 2021). CCSNe models underpredict [Mg/O], and the reason why is unknown.

3 THE EQUILIBRIUM APPROXIMATION

In the presence of metal-poor gas accretion and feedback-driven outflows, galaxies reach an equilibrium abundance in which production of new metals is balanced by losses to new stars and outflows (Larson 1972; Dalcanton 2007; Finlator & Davé 2008; Peeples & Shankar 2011; Lilly et al. 2013). While our galaxy is likely not in perfect equilibrium or described by a single, homogeneous chemical envirnoment, the equilibrium approximation is nevertheless useful in understanding yields and metallicity dependence of solar neighborhood stars (e.g. Johnson et al. 2022, 2023; Weinberg et al. 2017).

We assume a simple *one-zone* chemical evolution model (e.g. Tinsley 1980; Pagel 2009; Matteucci 2021). Newly produced metals are homogeneously and instantaneously mixed, so spatial dependence is neglected. We define M_X to be the mass of element X in the gas-phase, $\dot{M}_\star$ to be the star formation rate (in $\mathrm{M_\odot\,yr^{-1}}$), and η to be the mass loading factor $\eta \equiv \dot{M}_{\rm outflow}/\dot{M}_\star$ (representing the strength of outflows). A SSP returns a fraction r of their birth mass to the interstellar medium, due to ejected stellar envelopes.[9] Here, we will use α as a representative α-element, such as O or Mg. Given the IMF-averaged yield y_α, the rate of change in the gas-phase mass of α is a simple sum of sources and sinks,

$$\dot{M}_\alpha = y_\alpha\,\dot{M}_\star - \dot{M}_{\alpha,\,\rm remnants} - \dot{M}_{\alpha,\,\rm outflows} \tag{4}$$

where $y_\alpha\,\dot{M}_\star$ describes CCSNe enrichment. In terms of the return mass fraction of stars r, the mass lost to remnants is $Z_\alpha\,\dot{M}_\star\,(1-r)$. And, the outflows deplete mass at a rate $Z_\alpha\,\dot{M}_\star\,\eta$. (We assume the composition of outflows is the same as the interstellar medium.) Substituting for η and r,

$$\dot{M}_\alpha = y_\alpha\,\dot{M}_\star - (1+\eta-r)\,Z_\alpha\,\dot{M}_\star. \tag{5}$$

Assuming an exponentially declining star formation history $\dot{M}_\star \propto e^{-t/\tau_{\rm sfh}}$, the equilibrium abundance is derived analytically by setting $\dot{Z}_\alpha = 0$.

$$Z^{\rm eq}_\alpha(R) = \frac{y_\alpha}{1+\eta(R)-r-\tau_\star/\tau_{\rm sfh}}, \tag{6}$$

where $\tau_\star$ is the star formation rate. (η depends on R to create a metallicity gradient. See also Section 4 and Eq. 16.) In the special case of constant star formation, $\tau_{\rm sfh}\to\infty$, the denominator simplifies to $1+\eta-r$.

Likewise, for AGB stars,[10] Eq. 6 then becomes

$$Z^{\rm eq}_{\rm C}(R) = \frac{y^{\rm cc}_{\rm C} + y^{\rm agb}_{\rm C}}{1+\eta(R)-r-\tau_\star/\tau_{\rm sfh}} \tag{7}$$

And the equilibrium C/α abundance ratio is

$$\frac{Z^{\rm eq}_{\rm C}}{Z^{\rm eq}_\alpha} = \frac{y^{\rm cc}_{\rm C} + y^{\rm agb}_{\rm C}}{y_\alpha}. \tag{8}$$

Analogous to Johnson et al. (2023) arguments about N, the trends in abundance ratios are set by yield ratios in these GCE models. The effect of other GCE parameters (most importantly η) cancels. As a consequence, yield ratios should establish abundance ratio trends in models which assume a different normalization of element yields and mass-loading (see discussion below). This argument can also be inverted to infer yields from abundance ratio trends. To the extent that observed C and α trends reflect the equilibrium abundances in different Galactic regions, we can infer the CCSNe yield given an assumed AGB star yield (or vice versa). Inferring $y^{\rm cc}_{\rm C}$ from $y^{\rm agb}_{\rm C}$,

$$y^{\alpha}_{\rm C} = y^{\rm CC}_{\alpha}\,\frac{Z_{\rm C,\,eq}}{Z_{\alpha,\,\rm eq}} - y^{\rm agb}_{\rm C} \tag{9}$$

Rewriting this expression as a relative yield of C and Mg,

$$\frac{y^{\rm cc}_{\rm C}}{y_\alpha} = \left(\frac{Z_{\rm C}}{Z_\alpha}\right)_\odot 10^{[{\rm C}/\alpha]} - \frac{y^{\rm agb}_{\rm C}}{y_\alpha}. \tag{10}$$

3.1 Yield Models

As we will discuss in Section 5.5, the normalization of yields and η is degenerate. This can be observed in Eq. 8, where changes in η or the scaling of $y_{\rm C}/y_{\rm Mg}$ would not affect equilibrium trends. Furthermore, in Eq. 6, an increase in both $y_{\rm Mg}$ and η would leave $Z^{\rm eq}_{\rm Mg}$ unchanged. Our models here are unable to distinguish the overall scaling of yields and outflow mass loading. Choosing to keep $y_{\rm C}$ fixed reduces unnecessary free parameters. So, at solar metallicity, we set

$$y_{\rm C}(Z_\odot) = y^{\rm cc}_{\rm C} + y^{\rm agb}_{\rm C} = 0.005 \tag{11a}$$

$$\left(\frac{y_{\rm C}}{y^{\rm cc}_{\rm Mg}}\right)_{Z_\odot} = 2.7. \tag{11b}$$

This ratio results in an equilibrium abundance [C/Mg] = −0.09, which is consistent with the subgiant sample and is within ∼20% of the solar C/Mg mixture from Asplund et al. (2009).

In Section 5.3, we will show that none of the four AGB yield sets (`C11`, `K10`, `V13`, `K16`) produce enough C relative to this $y^{\rm cc}_{\rm C}$ value. So, we introduce normalization factors, $\alpha_{\rm AGB}$, and $\alpha_{\rm CC}$ which denote a multiplicative scaling of $y^{\rm cc}_{\rm C}$ and $y^{\rm agb}_{\rm C}$ respectively.

$$y^{\rm agb}_{\rm C} \to \alpha_{\rm agb}\,y^{\rm agb}_{\rm C} \tag{12a}$$

$$y^{\rm cc}_{\rm C} \to \alpha_{\rm cc}\,y^{\rm cc}_{\rm C} \tag{12b}$$

$$\alpha_{\rm CC} = \frac{y_{\rm C} - \alpha_{\rm agb}\,y^{\rm agb}_{\rm C}}{y^{\rm cc}_{\rm C}} \tag{12c}$$

[10] In detail, the AGB contribution requires integration over the SFH to account for the finite lifetimes of stars. However, for this exponential SFH, this effect is minimal, so we simply use $y^{\rm agb}_{\rm C}$ for the current AGB contribution.
[10] $r \approx 0.4$ for a Kroupa 2001 IMF.

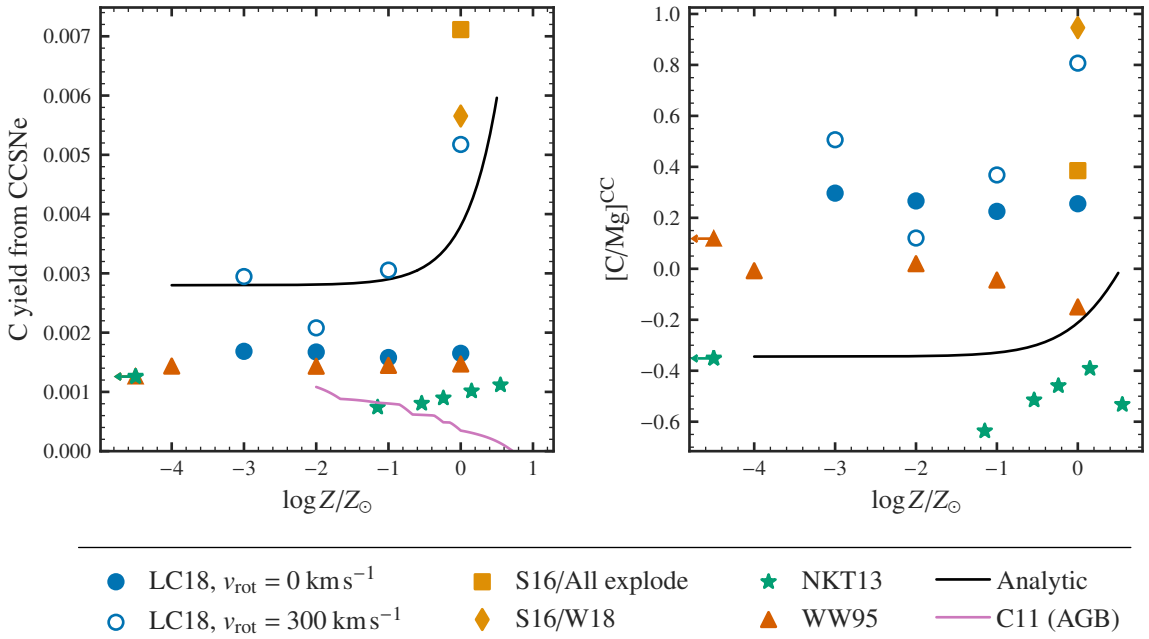

Figure 4. C yields from high-mass stars. **Left** The IMF-weighted CCSNe yield of C as a function of metallicity. **Right** The CCSNe [C/Mg] abundance ratio, defined in Eq. 3. The black line is the derived C yield from Section 3, $y_C^{cc} = 0.0028 + 0.001\,(Z/Z_\odot)$. Yields are shown for tables from Woosley & Weaver (1995, red triangles), Sukhbold et al. (2016, orange squares and diamonds), Nomoto et al. (2013, green stars), and Limongi & Chieffi (2018, blue circles). Sukhbold et al. (2016) report yields for different black hole landscapes, while Limongi & Chieffi (2018) provide yields at different rotational velocities. In the top panel, the pink line denotes y_C^{agb} from C11 for comparison. All models include wind yields.

Above, α_{cc} is dependent on the choice of α_{agb} to keep the total C yield constant.

In Section 5.3, we find that $\alpha_{agb} \approx 2.9$ for the C11 yield model. Using this AGB yield, we can now use Eq. 10 to find an estimate of y_C^{cc} as a function of metallicity. We show the values of y_C^{cc} we obtain from the subgiant sample in Fig. 5. From a regression analysis, we suggest here that

$$y_C^{cc} = 0.0028 + \zeta \left(\frac{Z}{Z_\odot}\right), \tag{13}$$

where $\zeta \approx 0.001$ describes the metallicity dependence.

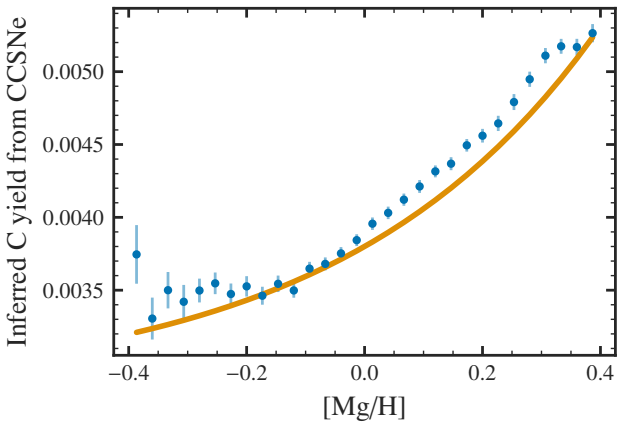

Figure 5. Inferred high-mass star C yields as a function of metallicity. We assume equilibrium and 3 × C11 AGB yields (orange curve, see discussion in Section 3). Blue points are the median value of y_C^{cc} for each bin in [Mg/H] with uncertainties based on the median absolute deviation.

3.2 Uncertainties

We only perform this analysis on the C11 yields because C11 has yields tables more finely sampled in metallicity than the other three AGB yield tables. As the metallicity range of the data is small ($-0.4 \lesssim$ [Mg/H] $\lesssim 0.4$), other models are more challenging to interpret in this range. Furthermore, the APOGEE observations may have systematics. Other measurements of C abundances (e.g. Vincenzo et al. 2021) have slight disagreements in the overall shape of the trend (see Section A). So, this expression of y_C^{cc}/y_{Mg}^{cc} depends on the chosen AGB yield table, the AGB fraction, and the dataset. Additionally, these yields will be systematically biased if the galaxy is out of equilibrium, for example, due to a recent starburst (Mor et al. 2019; Isern 2019). Further exploration could investigate the magnitude of these uncertainties, but we find that the qualitative conclusions are similar despite substantial variations in the assumptions here.

4 THE MULTI-ZONE MODEL

Classical, *one-zone* models of chemical evolution assume instantaneous mixing of metals in the star-forming interstellar medium (e.g. Matteucci 2021). This simple framework is a poor approximation of the Milky Way. The Galaxy evolves *inside-out*—where star formation is higher towards the center and in the early universe (Bird et al. 2013). Additionally, stars can migrate several kpc over their lifetimes, mixing different chemical environments across the galaxy (Bird et al.

2012; Sellwood & Binney 2002). For the rest of this paper, we focus on multi-zone models, which discretize the Galaxy into concentric rings in which stars move between. Our models extends the Johnson et al. (2021, hereafter J21) Milky Way model, run with the publicly available Versatile Integrator for Chemical Evolution (VICE). This model is described extensively in J21 and concisely summarized in Johnson et al. (2023). Here, we provide a brief overview of the relevant model components.

Our model is as follows. The Galaxy is divided into 200 rings, each 100 pc wide. Each ring has a separate stellar population and gas supply. We initially assume an inside-out SFH, where the star formation surface density $\Sigma_\star$ is given by

$$\dot{\Sigma}_\star \propto \left(1 - e^{-t/\tau_{\rm rise}}\right) e^{-t/\tau_{\rm sfh}}. \tag{14}$$

$\tau_{\rm rise} = 2$ Gyr describes when the star formation rate reaches a maximum, and $\tau_{\rm sfh}$ describes the decay timescale of star formation as a function of radius R. J21 derives $\tau_{\rm sfh}(R)$ through analysis of four integral field spectroscopy surveys in Sánchez (2020). At each R, the star formation history is normalized to match the stellar surface density gradient (Bland-Hawthorn & Gerhard 2016) and the total stellar mass reaches $5.17 \times 10^{10}\,{\rm M}_\odot$ (Licquia & Newman 2015). Star formation ends beyond a radius $R = 15.5$ kpc. The gas inflow is calculated to maintain our chosen SFH for each radius and time, using an extension of a Kennicutt-Schmidt law (Kennicutt 1998),

$$\dot{\Sigma}_\star \propto \begin{cases} \Sigma_{\rm gas} & 2 \times 10^7 \le \Sigma_{\rm gas} \\ (\Sigma_{\rm gas})^{3.6} & 5 \times 10^6 \le \Sigma_{\rm gas} < 2 \times 10^7 \\ (\Sigma_{\rm gas})^{1.7} & \Sigma_{\rm gas} < 5 \times 10^6 \end{cases} \tag{15}$$

where $\Sigma_{\rm gas}$ is measured in ${\rm M}_\odot$ kpc^{-2}. The scaling of this relationship varies with time due to the redshift dependence of $\tau_\star$ in molecular gas observed by Tacconi et al. (2018). We assume a Kroupa (2001) IMF.

To account for radial migration, J21 used the `h277` hydrodynamical simulation results (Christensen et al. 2012; Zolotov et al. 2012; Loebman et al. 2012; Brooks & Zolotov 2014). Simulation parameters are described in Bird et al. (2021). Each VICE single stellar population (SSP) is matched to an *analog* in `H277`, chosen to form at a similar time and radius R. By taking the change in radius ΔR of the analogs, the SSPs move to their final radii with a $\sqrt{\rm time}$ dependence. The $\Delta R \propto \sqrt{\rm time}$ dependence arises when migration proceeds as a consequence of the diffusion of angular momentum (Frankel et al. 2018, 2020). We do not account for radial gas flows. Using the results of a hydrodynamical simulation without modification limits the free parameters in the model; however, we am limited to one dynamical history. We do explore a normal-distribution random walk migration based on Frankel et al. (2018), without noticeable impacts on our results. All models shown here use the `h277`-based migration. The full impact of the details of a galaxy's dynamical history on its chemical evolution is still unknown.

As the strength of outflows controls the resulting α-element abundances, J21 create a metallicity gradient by defining

$$\eta(R) = r - 1 + \frac{y_\alpha^{\rm CC}}{Z_{\alpha,\odot}} 10^{(-0.08\,{\rm kpc}^{-1})(R - 4\,{\rm kpc}) + 0.3}. \tag{16}$$

This choice of $\eta(R)$ results in a [α/H] gradient consistent with Milky Way observations (e.g. Hayden et al. 2014; Weinberg et al. 2019; Frinchaboy et al. 2013).

5 RESULTS

5.1 Data Selection

We use the Roberts et al. (2023, in prep.) sample of APOGEE subgiants. Subgiant stars have not undergone FDU but have well-mixed atmospheres, so their atmospheric C and N abundances are still reflective of their birth abundances and do not need mixing corrections. We only compare the models to the low-α sequence unless otherwise specified. The selection criteria and differences between the samples are described in more detail in Appendix A.

5.2 Evolution of Carbon Abundances

Here, we present the time evolution of our fiducial model. In the next Sections, we will discuss the choice of parameters and agreement with observations. The fiducial model has the following qualitative characteristics of its C yields: (a) C is predominantly produced in CCSNe, (b) CCSNe produce more C at higher metallicities, and (c) AGB stars produce less C at higher metallicities. The fiducial model uses the `C11` AGB yield tables (see Section 2.1, and Table 1), and we amplify the `C11` yields by a factor of 2.9 such that AGB stars account for 20% of C at $Z = Z_\odot$.

We show the time evolution tracks of the fiducial model in Fig. 6 for [C/Mg]-[Mg/H] and [C/Mg]-[Mg/Fe]. Comparing [C/Mg] against [Mg/Fe] enables us to see the late-time evolution of C more clearly. Because of the extended delay time distribution of SNe Ia enrichment, [Fe/H] takes longer to reach equilibrium, and the late-time evolution is not as clustered as [Mg/H]. The evolution proceeds as follows. Initially, CCSNe dominate production. As $y_{\rm C}^{\rm cc}$ has strong metallicity dependence, [C/Mg] increases with time. Shortly thereafter, AGB stars contribute delayed C, increasing [C/Mg] even more steeply. As Mg begins to reach equilibrium, the [C/Mg] ratio plateaus as C approaches equilibrium. Finally, as $y_{\rm C}^{\rm agb}$ decreases or even becomes negative with higher metallicity, the [C/Mg] abundance may decline slightly. This is more evident in the lower panel of Fig. 6—while the [C/Mg]-[Mg/H] trend reaches equilibrium at ~5 Gyr, the [C/Mg]-[Mg/Fe] trend continues to evolve even until the present day, exposing the effect of the relative delay times of AGB stars and SNe Ia.

5.3 Low mass stellar yields

Discussion of negative yields.

Negative AGB yields cause a morphological change in the abundance trends. If the yields of low mass stars are negative, then at late times in a SSP, C abundances will decrease. This will appear as a downturn in the [C/Mg]-[Mg/Fe] abundance trends as [Mg/Fe] approaches solar values. As we do not observe this in the data, this is either obscured by star formation history (Seee eeee) or observational scatter.

Instead, if lower-intermediate mass AGB stars produce negative carbon yields, it is possible to observe this as a dip in the early parts of the [C/Mg]-[Mg/Fe] trend...

To parameterize the AGB contribution to C production, we define

$$f_{\rm AGB} \equiv \left.\frac{y_{\rm C}^{\rm agb}}{y_{\rm C}}\right|_{Z=Z_\odot}, \tag{17}$$

where $y_{\rm C}^{\rm agb}$ includes the multiplicative factor $\alpha_{\rm AGB}$ as defined in Eq. 12. Fig. 7 compares the `K10`, `K16`, `C11`, and `V13` yield models. We use the published, unscaled yield tables ($\alpha_{\rm AGB} = 1$) for Fig. 7.

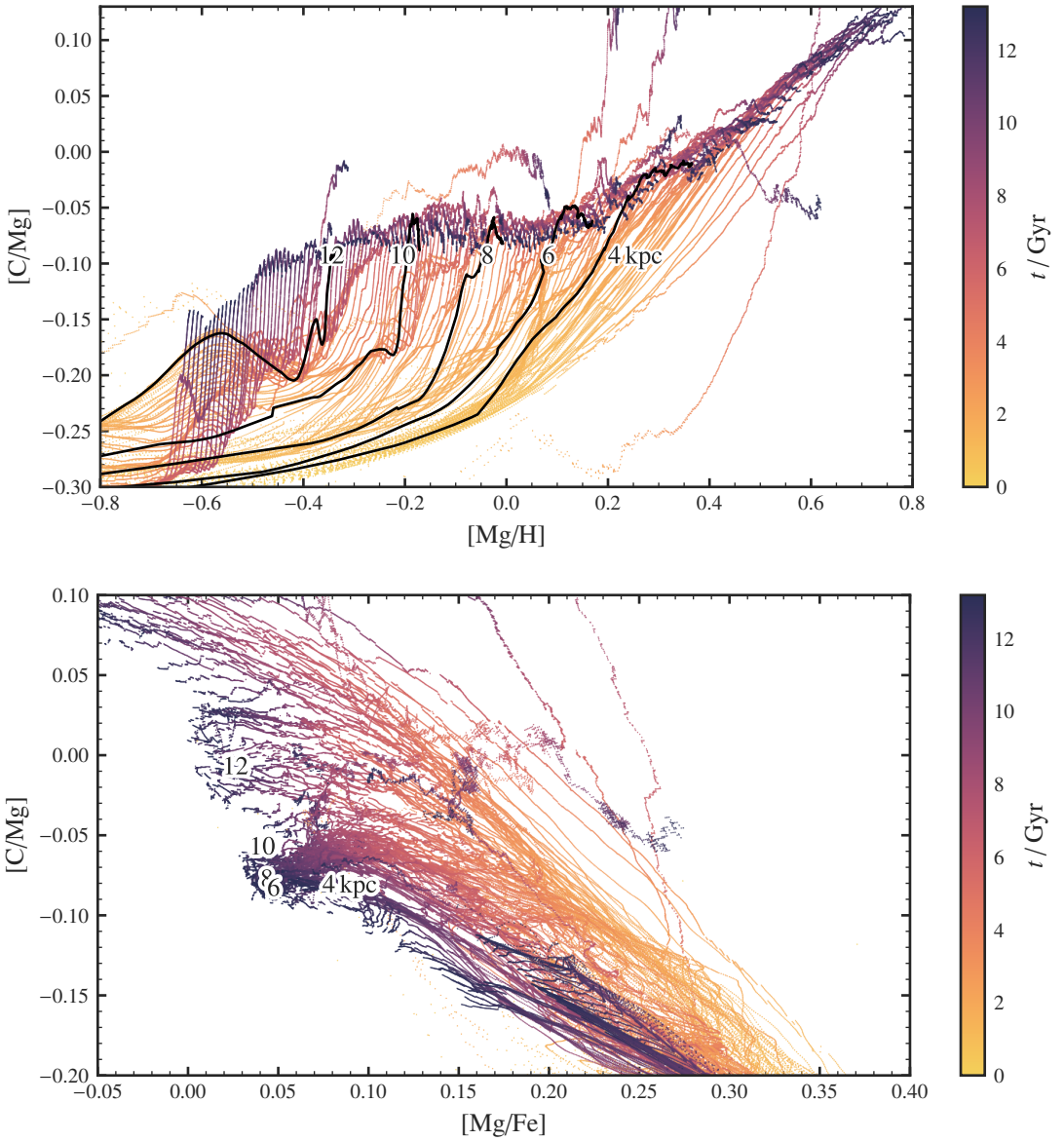

Figure 6. Time evolution of gas-phase C abundances in our fiducial model. **Top:** Evolutionary tracks parameterized by time at fixed Galactocentric radius in the [C/Mg]-[Mg/H] and [C/Mg]-[Mg/Fe] planes. **Bottom:** Snapshots of the gas-phase [C/Mg]-[Mg/H] and [C/Mg]-[Mg/Fe] trend, parameterized by radius at a fixed time.

As the highest AGB yield at solar, K10 is only $y_C^{agb} = 0.000585$, $f_{AGB} \leq 0.12$ for all models. Massive stars dominate C production with unscaled yields. While it is easy to modify the AGB yields in our model, their small contribution reduces the effect. We leave a more detailed discussion of the effects of AGB models for Appendix 5.3 and use C11 yields hereafter.

Next, we investigate adjustments to the AGB yield fraction f_{AGB} and the CCSNe metallicity dependence ζ in Fig. 8. On the top panel of Fig. 8, we plot models with varying y_C^{cc} metallicity dependence. As discussed in Section 3, the [C/Mg]-[Mg/H] trend is approximated by equilibrium, so the trends of these have steeper [C/Mg]-[Mg/H] corresponding to steeper metallicity dependence. However, [C/Mg]-[Mg/Fe] is minimally affected by these changes since CCSNe occurs on much shorter timescales than SNe Ia and AGB enrichment.

In the bottom panel of Fig. 8, we plot three models with different AGB fractions while using C11 yields. The [C/Mg]-[Mg/Fe] relationship is set by f_{AGB} because a specific amount of C must be released at a delayed time to match the SNe Ia production of Fe and increase [C/Mg] as [Mg/Fe] decreases to reproduce the data. Increased f_{AGB} results in a decreased slope in [C/Mg]-[Mg/H], owing to the negative metallicity dependence of y_C^{agb}. So while [C/Mg]-[Mg/H] alone cannot differentiate models which vary f_{AGB} and ζ correspondingly, [C/Mg]-[Mg/Fe] provides information on f_{AGB}. So, we can use [C/Mg]-[Mg/Fe] to estimate $f_{AGB} \approx 0.2$, and then choose ζ to match [C/Mg]-[Mg/H].

One source of theoretical uncertainty in this result is that the SNe Ia yield and delay time distributions have their own uncertainties. We discuss variations in y_{Fe}^{Ia} in Appendix 5.3, and find that the qualitative conclusions are largely unaffected. I, therefore, focus on the choices of $y_{Fe}^{Ia} = 0.00214$ and a $t^{-1.1}$ delay time distribution

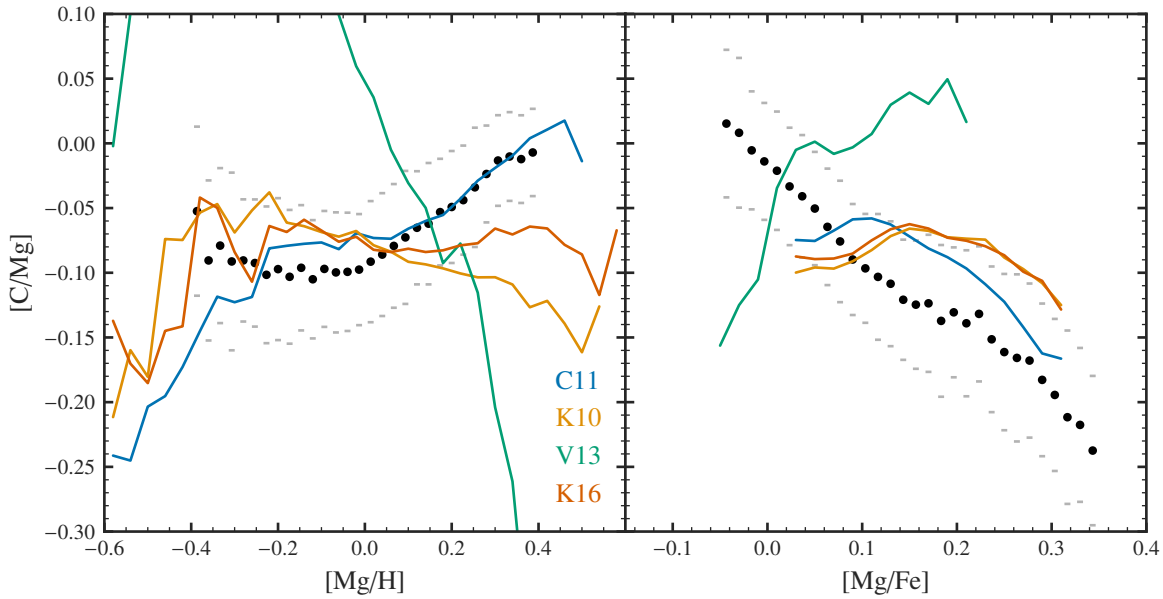

Figure 7. Stellar abundance trends in our model, assuming metallicity independent y_C^{cc}. Colored lines quantify the median [C/Mg] in bins of [Mg/H] for our four AGB yield models from the literature (see Section 2.1). Black points and grey dashes represent the median and standard deviations of [C/Mg] for each [Mg/H] bin in the Roberts et al. (2023, in prep.) sample. In the right panel, we show the trends only for stars where $-0.15 \leq$ [Mg/H] ≤ -0.05.

Table 2. For each AGB yield set, the IMF-averaged AGB C yield at solar metallicity $y_{C,0}^{AGB}$ and the multiplicative factor reaches an AGB contribution of 20% $\alpha_{AGB,20}$.

AGB Model	$y_{C,0}^{AGB}$	$\alpha_{AGB,20}$
C11	0.000347	2.9
K10	0.000585	1.7
V13	0.000060	16.5
K16	0.000421	2.4

choices from the fiducial model here. In short, the scaling of the trend and metallicity dependence of C (as seen in the [C/Mg]-[Mg/H] trend) gives information on the total C yield and the behavior of CCSNe (as the dominating producer of C), the [C/Mg]-[Mg/Fe] trend exposes the delayed effect of C from AGB contribution.

5.4 Star Formation History

Here, we consider a *lateburst* model, created by multiplying our fiducial inside-out SFH with a Gaussian.

$$\dot{\Sigma}_{\rm lateburst} \propto \dot{\Sigma}_{\rm inside-out}\left(1 + A\, e^{-(t-\tau_{\rm burst})^2/2\sigma^2_{\rm burst}}\right) \tag{18}$$

$A = 1.5$ represents the amplitude of the birth, $\tau_{\rm burst} = 10.8$ Gyr is the time where the burst is strongest, and $\sigma_{\rm burst} = 1$ Gyr is the width of the burst. We also consider an *earlyburst* model as a slight variation of the lateburst, where the burst is instead exponential and placed at $t_1 = 5$ Gyr.

$$\dot{\Sigma}_{\rm earlyburst} \propto \dot{\Sigma}_{\rm inside-out} + \begin{cases} A\, e^{-(t-t_1)/\tau_{\rm burst}} & t_1 < t \\ 0 & t < t_1 \end{cases} \tag{19}$$

where we take the burst duration, $\tau_{\rm burst} = 1$ Gyr in this case. This approximately corresponds to the Gaia-Encelidus merger, inducing higher star formation in the Milky Way (Spitoni et al. 2021; Bonaca et al. 2020; Helmi et al. 2018).

Fig. 9 shows three models with these alternate SFH. Changes to the SFH leave [C/Mg]-[Mg/H] unchanged, but they do introduce slight variation in [C/Mg]-[Mg/Fe]. Models with higher AGB fractions are more sensitive to variations in the SFH. The late burst models result in [C/Mg] continuing to increase at low [Mg/Fe], but also introduce a dip not present in the data. Additionally, the early burst reproduces the slight break between the low and high α sequences, but overshoots equilibrium more severely than the fiducial model. In general, any of these SFHs are consistent with this model.

5.5 Degeneracies

Radial migration doesn't matter...

GCE models of the Milky Way fall into two classes—those which incorporate significant mass-loading (e.g., this work) and those which neglect mass-loading but lower effective yield to match observed abundances (e.g. Minchev et al. 2013, 2014; Spitoni et al. 2019, 2020, 2021). An increase in stellar yields has a nearly identical effect as a decrease in the mass-loading factor η (see Appendix B of Johnson et al. 2022). The equilibrium arguments discussed in Section 3 suggest however that abundance ratios are independent of the choice of normalization and the value of η. I, therefore, expect our results regarding the relative yield y_C/y_{Mg} and its metallicity dependence to extend to the other class of models omitting mass loading. We demonstrate this further here.

The theoretical motivation for decreasing yields is the uncertainty in stellar explodability. If fewer high-mass stars explode, then the yields will be reduced by some factor. Additionally, some fraction of supernovae ejecta may be lost directly to an outflow, lowering effective yields. To explore reduced outflow models, we lower both η and all yields by the same factor to leave the equilibrium abundances unchanged.

Fig. 10 shows models with variations of the mass loading strength.

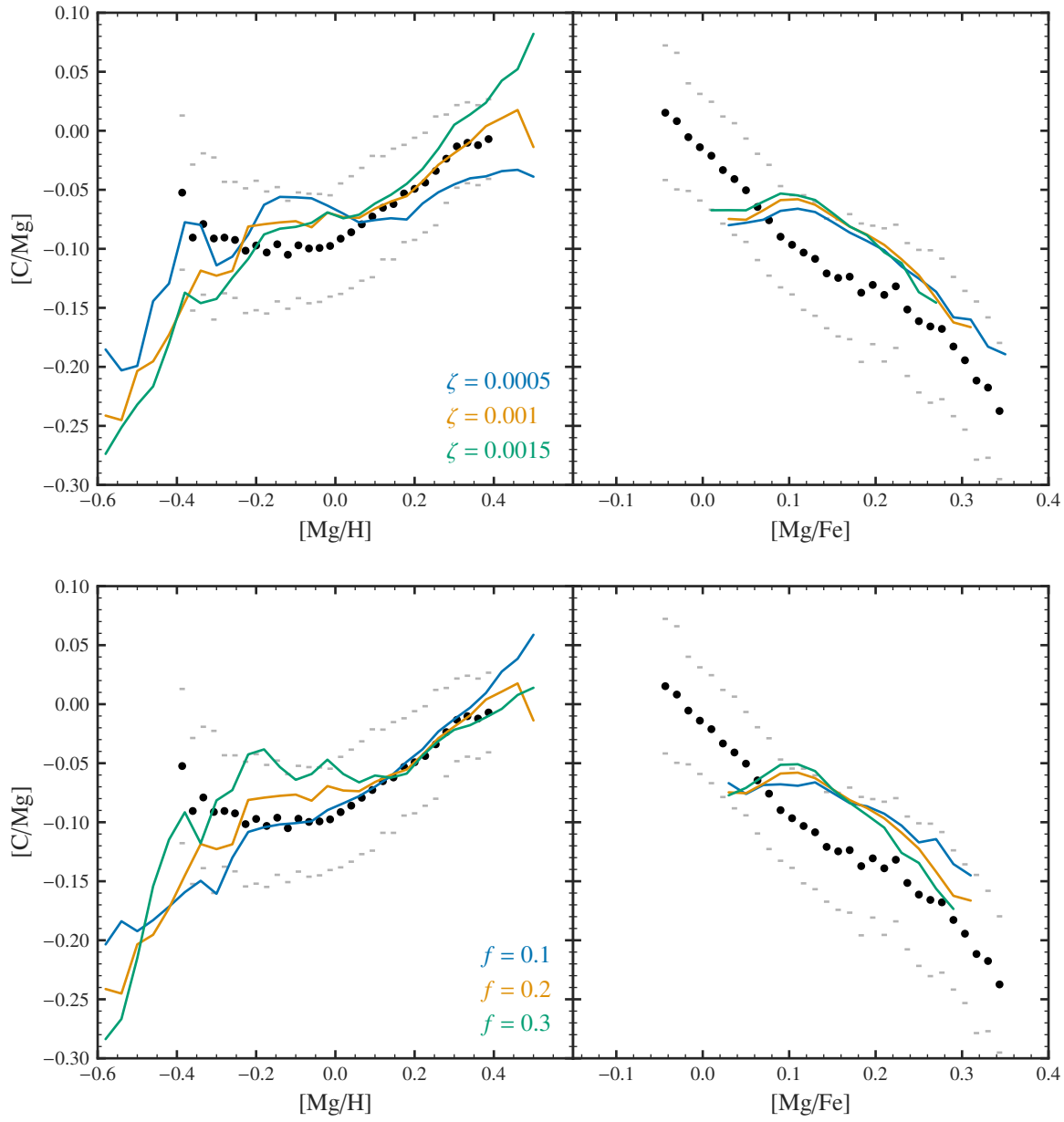

Figure 8. Similar to Fig. 7 except the top plot shows the fiducial model with lower and higher values of ζ, the metallicity dependence of y_C^{cc}. The bottom plot shows models with f_{AGB} =0.1, 0.2, and 0.4. Both the f_{AGB} and ζ influence [C/Mg]-[Mg/H], but only f_{AGB} has a significant impact on [C/Mg]-[Mg/Fe].

While changing the value of η affects the metallicity distribution of stars, all of the models in Fig. 10 still evolve along the same path. Our model is unable to differentiate a uniform decrease in both outflows and yields.

5.6 Gas-Phase Abundances

C abundances are challenging to measure. When a star enters the Red Giant Branch (RGB), material from the CNO-processed core is mixed with the envelope in first dredge up, enhancing N and depleting C (Iben 1967; Vincenzo et al. 2021; Karakas & Lattanzio 2014). Measurements of these evolved stars' atmospheres will no longer reflect their birth abundances. Additionally, gas-phase measurements of C are extremely limited as C lacks strong lines in HII regions (Skillman et al. 2020).

As an additional test of the model, we next compare the model predictions against gas-phase measurements. Fig. 12 shows the fiducial model's gas-phase predictions compared to observations of the Milky Way and extragalactic HII regions, halo stars, and DLA systems. The model is broadly consistent with observations, where the model at $t = 2$ Gyr approximates the slope of dwarf galaxies and halo stars. The increase of C/O at higher metallicities is also consistent with the high C/O abundances measured in extragalactic HII regions. Our model does not extend to very low metallicity, where the slope of the trend inverts, but broadly explains observations above [O/H] $\gtrsim -1$.

Mg measurements are more reliable, but O abundances are easier to measure in HII regions. So while we use Mg as the representative

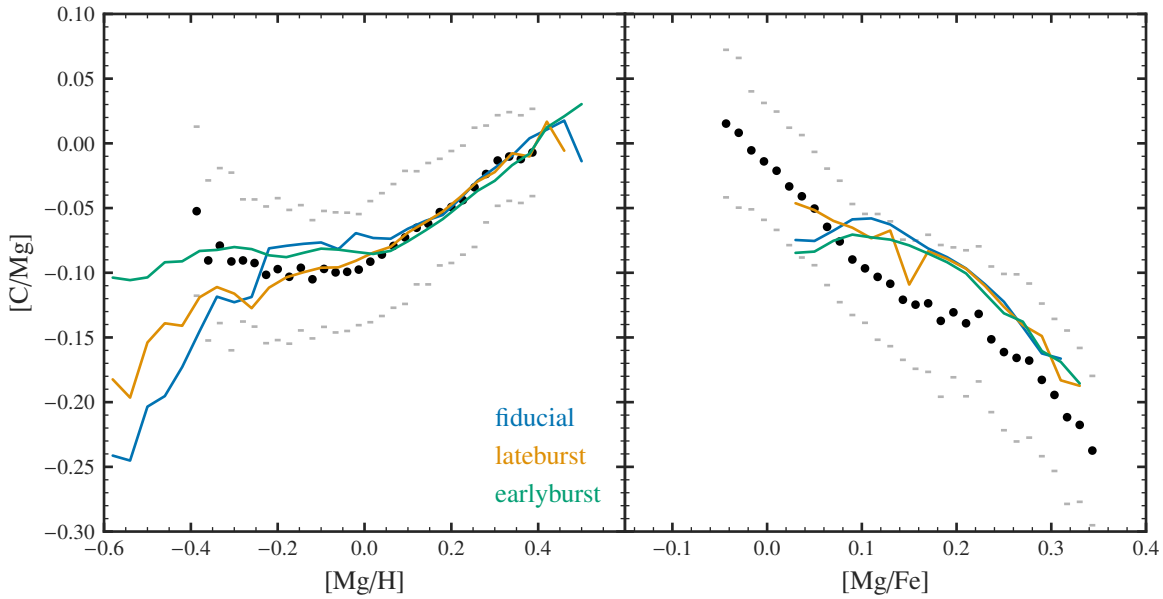

Figure 9. Similar to Fig. 7 but comparing the fiducial model to alternate star formation histories (see Section 5.4).

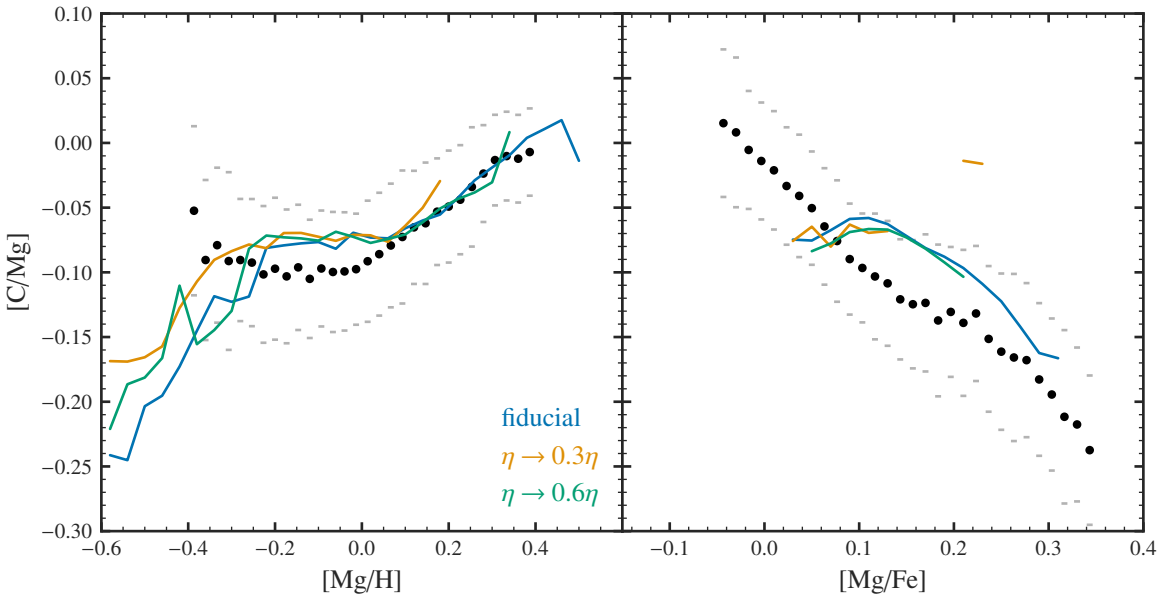

Figure 10. Similar to Fig. 7 but comparing the fiducial model to reduced mass loading models (see Section 5.5). Both yields and mass-loading are adjusted correspondingly such that the equilibrium abundances are unchanged.

alpha for stellar abundances, we instead use O when comparing gas-phase abundances. As we assume [Mg/O] = 0, our model is independent of the choice of the alpha

Measurements of C abundances in the gas-phase are challenging. In HII regions, C/O abundance ratios are measured with either recombination lines or collisional excitation lines. However C lacks strong collisional excitation lines, and recombination lines fall in the ultraviolet without nearby reference H lines (Skillman et al. 2020). Additionally, recombination and collisional excitation measurements disagree by a factor of ~2 (García-Rojas & Esteban 2007). Variations in the SFHs may furthermore increase scatter, as AGB are a delayed source of C.

The decreasing [C/O] abundance at very-low metallicities is likely due to population III stellar yields (e.g. Hirschi 2007), as suggested by Cooke et al. (2017) and Frebel & Norris (2015). agb stars cannot explain the increase in C yields at low metallicity in the DLA sample as the evolutionary timescales of DLAs are shorter than the typical delay time distribution of AGB stars.

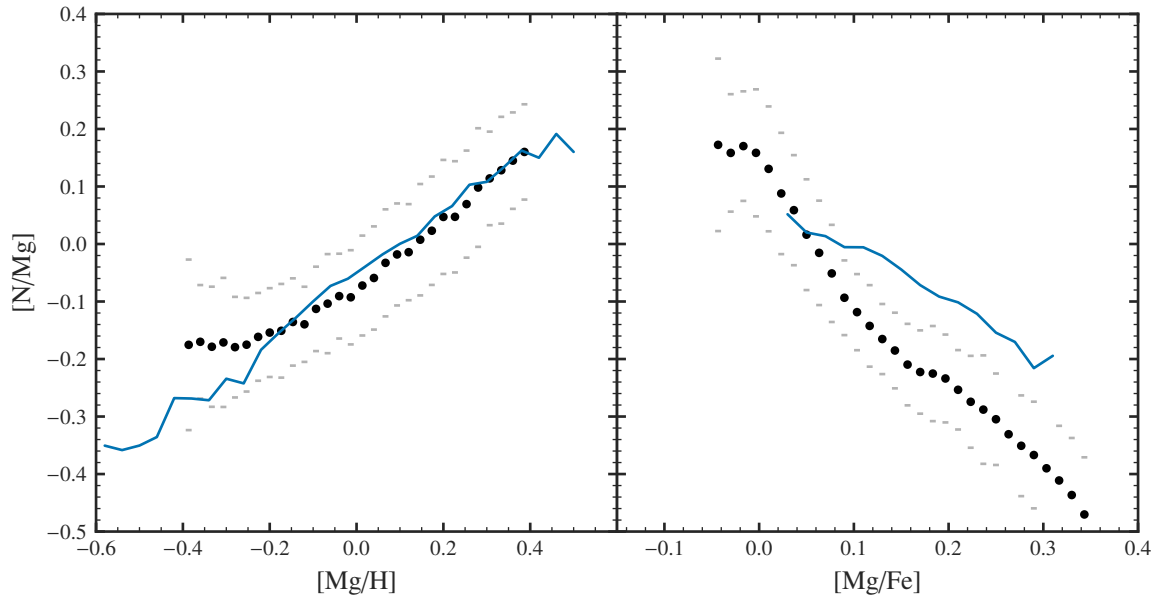

Figure 11. Similar to Fig. 7, except comparing [C/N] from the fiducial model only. N yields are adapted from Johnson et al. (2023). (See also Table 1.)

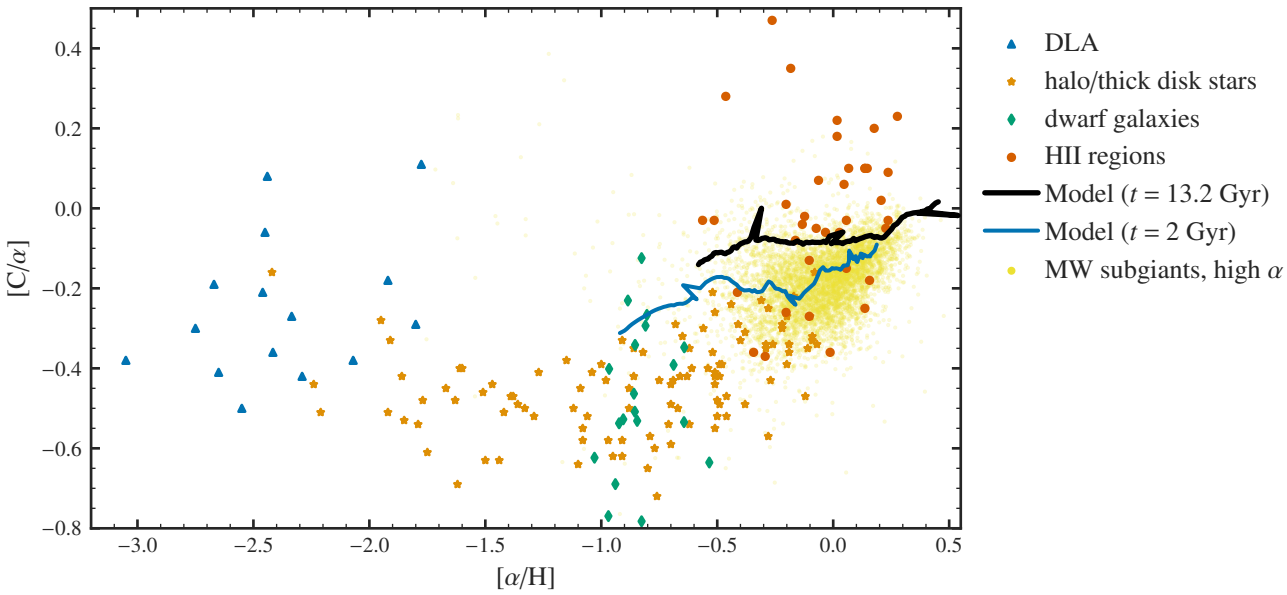

Figure 12. Gas-phase C abundances. We plot our model at $t = 2$ Gyr and present day as thick solid lines. Points represent measurements in HII regions (pink circles; Skillman et al. 2020; Esteban et al. 2002, 2009, 2014, 2019) DLA systems (blue triangles; Ellison et al. 2010; Srianand et al. 2010; Dutta et al. 2014; Dessauges-Zavadsky et al. 2003; Pettini et al. 2008; Morrison et al. 2016; Cooke et al. 2017), dwarf galaxies (red diamonds; Berg et al. 2019), Milky Way halo and thick disk stars (green stars; Nissen et al. 2014; Fabbian et al. 2009), and Milky Way high-α stars (yellow points; Robert et al. 2023, in prep.).

6 CONCLUSIONS

In this work, we investigate the role of C yields on the predictions of multi-zone GCE models. Johnson et al. (2023) performed a similar analysis focusing on N. They found that matching the observed relationship between N and O abundances[11] requires relative N and O yields from simple stellar populations with a roughly linear dependence on metallicity (i.e. $y_N/y_O \propto Z$). Here, we perform a similar analysis on C.

Though CCSNe C yields are poorly understood, we adopt an equi-

[11] e.g. Henry et al. (2000); Pilyugin et al. (2010); Berg et al. (2012, 2020); Skillman et al. (2020); Izotov et al. (2012); James et al. (2015); Dopita et al. (2016).

librium approximation and determine a functional form that approximately matches trends in APOGEE subgiant and is consistent with high-mass nucleosynthesis models. Variations of the metallicity dependence of this CCSNe yield affect trends in [C/Mg]-[Mg/H] but do not affect trends in [C/Mg]-[Mg/Fe] (when taking a slice in [Mg/H]). As all theoretical AGB C yields decrease with metallicity, increasing the AGB fraction causes the [C/Mg]-[Mg/H] trend to flatten. However, the [C/Mg]-[Mg/Fe] trend is sensitive to the AGB fraction. From this, we estimate that AGB stars contribute ~20% of total C abundance at solar metallicity. The remaining ~80% of C comes from high-mass stars with a metallicity dependent yield of $y_{\rm C}^{\rm cc}/y_{\rm Mg}^{\rm cc} = 1.51 + 0.54(Z/Z_{\odot})$. This metallicity dependence is roughly consistent with rotating stellar yields.

We additionally explore variations of the assumed SFH and outflow mass-loading factor η. We find that alternate SFHs can slightly affect [C/Mg]-[Mg/Fe], but [C/Mg]-[Mg/H] is mostly unaffected. Decreasing both outflows and yields by the same factor leaves the [C/Mg]-[Mg/H] and [C/Mg]-[Mg/Fe] trends unaffected. These constraints on the relative yields of C, O, and Mg are robust against variations in η.

Finally, we compare our model against gas-phase measurements and metal-poor stars. While our model was built on data near solar metallicity, observations of very low metallicity, high redshift damped Lyman-α systems indicate higher C/O ratios (Cooke et al. 2017), consistent with yields from population III stars (e.g. Hirschi 2007). Population III stars, CCSNe and AGBstars altogether explain the observed evolutionary history of C.

These C yield constraints provide a useful benchmark for stellar evolution models. C yields are sensitive to poorly understood processes, including mass-loss prescriptions, explodability, nuclear cross sections, convection, and stellar structure. Future spectroscopic surveys combined with Gaia kinematics (Gaia Collaboration et al. 2016) will continue to enhance our understanding of chemical evolution. Both the Sloan Digital Sky Survey V's Milky Way Mapper program (SDSS-V/MWM) (Kollmeier et al. 2017) and the Dark Energy Spectroscopic Instrument (DESI) Milky Way survey (DESI Collaboration et al. 2016; Cooper et al. 2022) will each measure spectra of upwards 6,000,000 Milky Way stars. These larger samples will enable similar work to tighten constraints on stellar models and our understanding of galaxy structure and evolution.

ACKNOWLEDGEMENTS

Here you can thank helpful colleagues, acknowledge funding agencies, telescopes and facilities used etc. Try to keep it short.

Software that has contributed to this work included VICE (Johnson & Weinberg 2020; Johnson et al. 2021), `matplotlib` (Hunter 2007), `scipy` (Virtanen et al. 2020), `IPython` (Pérez & Granger 2007), `pandas` (pandas development team 2020), `numpy` (Harris et al. 2020), `astropy` (Astropy Collaboration et al. 2013, 2018, 2022), and `seaborn` (Waskom 2021) . Additionally, we thank Ohio Supercomputer Center (1987) for the use of its facilities for the simulations.

DATA AVAILABILITY

The inclusion of a Data Availability Statement is a requirement for articles published in MNRAS. Data Availability Statements provide a standardised format for readers to understand the availability of data underlying the research results described in the article. The statement may refer to original data generated in the course of the study or to third-party data analysed in the article. The statement should describe and provide means of access, where possible, by linking to the data or providing the required accession numbers for the relevant databases or DOIs.

REFERENCES

Abdurro'uf et al., 2022, ApJS, 259, 35
Adelberger E. G., et al., 2011, Reviews of Modern Physics, 83, 195
Asplund M., Grevesse N., Sauval A. J., Scott P., 2009, ARA&A, 47, 481
Astropy Collaboration et al., 2013, A&A, 558, A33
Astropy Collaboration et al., 2018, AJ, 156, 123
Astropy Collaboration et al., 2022, ApJ, 935, 167
Bensby T., Feltzing S., 2006, MNRAS, 367, 1181
Berg D. A., et al., 2012, ApJ, 754, 98
Berg D. A., Erb D. K., Henry R. B. C., Skillman E. D., McQuinn K. B. W., 2019, ApJ, 874, 93
Berg D. A., Pogge R. W., Skillman E. D., Croxall K. V., Moustakas J., Rogers N. S. J., Sun J., 2020, ApJ, 893, 96
Bird J. C., Kazantzidis S., Weinberg D. H., 2012, MNRAS, 420, 913
Bird J. C., Kazantzidis S., Weinberg D. H., Guedes J., Callegari S., Mayer L., Madau P., 2013, ApJ, 773, 43
Bird J. C., Loebman S. R., Weinberg D. H., Brooks A. M., Quinn T. R., Christensen C. R., 2021, MNRAS, 503, 1815
Bland-Hawthorn J., Gerhard O., 2016, ARA&A, 54, 529
Bonaca A., et al., 2020, ApJ, 897, L18
Brooks A. M., Zolotov A., 2014, ApJ, 786, 87
Chiappini C., Romano D., Matteucci F., 2003, MNRAS, 339, 63
Christensen C., Quinn T., Governato F., Stilp A., Shen S., Wadsley J., 2012, MNRAS, 425, 3058
Cooke R. J., Pettini M., Steidel C. C., 2017, MNRAS, 467, 802
Cooper A. P., et al., 2022, arXiv e-prints, p. arXiv:2208.08514
Cristallo S., et al., 2011, ApJS, 197, 17
Cristallo S., Straniero O., Piersanti L., Gobrecht D., 2015, ApJS, 219, 40
DESI Collaboration et al., 2016, arXiv e-prints, p. arXiv:1611.00036
Dalcanton J. J., 2007, ApJ, 658, 941
Dearborn D. S. P., Tinsley B. M., Schramm D. N., 1978, ApJ, 223, 557
Dessauges-Zavadsky M., Péroux C., Kim T. S., D'Odorico S., McMahon R. G., 2003, MNRAS, 345, 447
Dopita M. A., Kewley L. J., Sutherland R. S., Nicholls D. C., 2016, Ap&SS, 361, 61
Dutta R., Srianand R., Rahmani H., Petitjean P., Noterdaeme P., Ledoux C., 2014, MNRAS, 440, 307
Ellison S. L., Prochaska J. X., Hennawi J., Lopez S., Usher C., Wolfe A. M., Russell D. M., Benn C. R., 2010, MNRAS, 406, 1435
Esteban C., Peimbert M., Torres-Peimbert S., Rodríguez M., 2002, ApJ, 581, 241
Esteban C., Bresolin F., Peimbert M., García-Rojas J., Peimbert A., Mesa-Delgado A., 2009, ApJ, 700, 654
Esteban C., García-Rojas J., Carigi L., Peimbert M., Bresolin F., López-Sánchez A. R., Mesa-Delgado A., 2014, MNRAS, 443, 624
Esteban C., García-Rojas J., Arellano-Córdova K. Z., Méndez-Delgado J. E., 2019, arXiv e-prints, p. arXiv:1905.10129
Fabbian D., Nissen P. E., Asplund M., Pettini M., Akerman C., 2009, A&A, 500, 1143
Finlator K., Davé R., 2008, MNRAS, 385, 2181
Frankel N., Rix H.-W., Ting Y.-S., Ness M., Hogg D. W., 2018, ApJ, 865, 96
Frankel N., Sanders J., Ting Y.-S., Rix H.-W., 2020, ApJ, 896, 15
Frebel A., Norris J. E., 2015, ARA&A, 53, 631
Frinchaboy P. M., et al., 2013, ApJ, 777, L1
Gaia Collaboration et al., 2016, A&A, 595, A1
García Pérez A. E., et al., 2016, AJ, 151, 144
García-Rojas J., Esteban C., 2007, ApJ, 670, 457
Gilroy K. K., 1989, ApJ, 347, 835
Griffith E. J., Sukhbold T., Weinberg D. H., Johnson J. A., Johnson J. W., Vincenzo F., 2021, ApJ, 921, 73

Harris C. R., et al., 2020, Nature, 585, 357
Hasselquist S., et al., 2019, ApJ, 871, 181
Hayden M. R., et al., 2014, AJ, 147, 116
Helmi A., Babusiaux C., Koppelman H. H., Massari D., Veljanoski J., Brown A. G. A., 2018, Nature, 563, 85
Henry R. B. C., Edmunds M. G., Köppen J., 2000, ApJ, 541, 660
Hirschi R., 2007, A&A, 461, 571
Hunter J. D., 2007, Computing in Science & Engineering, 9, 90
Iben Icko J., 1967, ARA&A, 5, 571
Isern J., 2019, ApJ, 878, L11
Izotov Y. I., Thuan T. X., Guseva N. G., 2012, A&A, 546, A122
James B. L., Koposov S., Stark D. P., Belokurov V., Pettini M., Olszewski E. W., 2015, MNRAS, 448, 2687
Johnson J. W., Weinberg D. H., 2020, MNRAS, 498, 1364
Johnson J. W., et al., 2021, MNRAS, 508, 4484
Johnson J. W., et al., 2022, arXiv e-prints, p. arXiv:2210.01816
Johnson J. W., Weinberg D. H., Vincenzo F., Bird J. C., Griffith E. J., 2023, MNRAS, 520, 782
Karakas A. I., 2010, MNRAS, 403, 1413
Karakas A. I., Lattanzio J. C., 2014, Publ. Astron. Soc. Australia, 31, e030
Karakas A. I., Lugaro M., 2016, ApJ, 825, 26
Karakas A. I., Lugaro M., Carlos M., Cseh B., Kamath D., García-Hernández D. A., 2018, MNRAS, 477, 421
Kennicutt Robert C. J., 1998, ARA&A, 36, 189
Kobayashi C., Karakas A. I., Lugaro M., 2020, ApJ, 900, 179
Kollmeier J. A., et al., 2017, arXiv e-prints, p. arXiv:1711.03234
Korn A. J., Grundahl F., Richard O., Mashonkina L., Barklem P. S., Collet R., Gustafsson B., Piskunov N., 2007, ApJ, 671, 402
Kroupa P., 2001, MNRAS, 322, 231
Larson R. B., 1972, Nature Physical Science, 236, 7
Larson R. B., 1974, MNRAS, 166, 585
Licquia T. C., Newman J. A., 2015, ApJ, 806, 96
Lilly S. J., Carollo C. M., Pipino A., Renzini A., Peng Y., 2013, ApJ, 772, 119
Limongi M., Chieffi A., 2018, ApJS, 237, 13
Lind K., Korn A. J., Barklem P. S., Grundahl F., 2008, A&A, 490, 777
Loebman S. R., Ivezić Ž., Quinn T. R., Governato F., Brooks A. M., Christensen C. R., Jurić M., 2012, ApJ, 758, L23
Majewski S. R., et al., 2017, AJ, 154, 94
Maoz D., Mannucci F., Brandt T. D., 2012, MNRAS, 426, 3282
Martig M., et al., 2016, MNRAS, 456, 3655
Masseron T., Gilmore G., 2015, MNRAS, 453, 1855
Matteucci F., 2021, A&ARv, 29, 5
Minchev I., Chiappini C., Martig M., 2013, A&A, 558, A9
Minchev I., Chiappini C., Martig M., 2014, A&A, 572, A92
Mor R., Robin A. C., Figueras F., Roca-Fàbrega S., Luri X., 2019, A&A, 624, L1
Morrison S., Kulkarni V. P., Som D., DeMarcy B., Quiret S., Péroux C., 2016, ApJ, 830, 158
Nissen P. E., Chen Y. Q., Carigi L., Schuster W. J., Zhao G., 2014, A&A, 568, A25
Nomoto K., Kobayashi C., Tominaga N., 2013, ARA&A, 51, 457
Ohio Supercomputer Center 1987, Ohio Supercomputer Center, `http://osc.edu/ark:/19495/f5s1ph73`
Pagel B. E. J., 2009, Nucleosynthesis and Chemical Evolution of Galaxies, 2 edn. Cambridge University Press, doi:10.1017/CBO9780511812170
Paxton B., Bildsten L., Dotter A., Herwig F., Lesaffre P., Timmes F., 2011, ApJS, 192, 3
Peeples M. S., Shankar F., 2011, MNRAS, 417, 2962
Pérez F., Granger B. E., 2007, Computing in Science and Engineering, 9, 21
Pettini M., Zych B. J., Steidel C. C., Chaffee F. H., 2008, MNRAS, 385, 2011
Pilyugin L. S., Vílchez J. M., Thuan T. X., 2010, ApJ, 720, 1738
Prantzos N., Abia C., Limongi M., Chieffi A., Cristallo S., 2018, MNRAS, 476, 3432
Romano D., 2022, A&ARv, 30, 7
Romano D., Karakas A. I., Tosi M., Matteucci F., 2010, A&A, 522, A32
Rybizki J., Just A., Rix H.-W., 2017, A&A, 605, A59
Sánchez S. F., 2020, ARA&A, 58, 99
Sellwood J. A., Binney J. J., 2002, MNRAS, 336, 785
Skillman E. D., Berg D. A., Pogge R. W., Moustakas J., Rogers N. S. J., Croxall K. V., 2020, ApJ, 894, 138
Souto D., et al., 2018, ApJ, 857, 14
Souto D., et al., 2019, ApJ, 874, 97
Spitoni E., Silva Aguirre V., Matteucci F., Calura F., Grisoni V., 2019, A&A, 623, A60
Spitoni E., Verma K., Silva Aguirre V., Calura F., 2020, A&A, 635, A58
Spitoni E., et al., 2021, A&A, 647, A73
Srianand R., Gupta N., Petitjean P., Noterdaeme P., Ledoux C., 2010, MNRAS, 405, 1888
Sukhbold T., Ertl T., Woosley S. E., Brown J. M., Janka H. T., 2016, ApJ, 821, 38
Tacconi L. J., et al., 2018, ApJ, 853, 179
Tinsley B. M., 1979, ApJ, 229, 1046
Tinsley B. M., 1980, Fundamentals Cosmic Phys., 5, 287
Ventura P., Di Criscienzo M., Carini R., D'Antona F., 2013, MNRAS, 431, 3642
Ventura P., Dell'Agli F., Schneider R., Di Criscienzo M., Rossi C., La Franca F., Gallerani S., Valiante R., 2014, MNRAS, 439, 977
Ventura P., Karakas A., Dell'Agli F., García-Hernández D. A., Guzman-Ramirez L., 2018, MNRAS, 475, 2282
Ventura P., Dell'Agli F., Lugaro M., Romano D., Tailo M., Yagüe A., 2020, A&A, 641, A103
Vincenzo F., et al., 2021, arXiv e-prints, p. arXiv:2106.03912
Virtanen P., et al., 2020, Nature Methods, 17, 261
Waskom M. L., 2021, Journal of Open Source Software, 6, 3021
Weinberg D. H., Andrews B. H., Freudenburg J., 2017, ApJ, 837, 183
Weinberg D. H., et al., 2019, ApJ, 874, 102
Weinberg D. H., et al., 2022, ApJS, 260, 32
Woosley S. E., Weaver T. A., 1995, ApJS, 101, 181
Zolotov A., et al., 2012, ApJ, 761, 71
pandas development team T., 2020, pandas-dev/pandas: Pandas, doi:10.5281/zenodo.3509134, `https://doi.org/10.5281/zenodo.3509134`

APPENDIX A: THE SUBGIANT SAMPLE

As the primary observational constraint, we use the criteria outlined in Roberts et al. (2023, in prep.) to create a sample of subgiant from APOGEE DR17 (Majewski et al. 2017). apogee is part of the Sloan Digital Sky Survey and measures high-resolution spectra of thousands of stars Abdurro'uf et al. (2022). Chemical abundances are determined from the APOGEE Stellar Parameter and Chemical Abundance Pipeline (ASPCAP) (García Pérez et al. 2016).

Photospheric C and N abundances in subgiant are reflective of their birth abundances (Gilroy 1989; Korn et al. 2007; Lind et al. 2008; Souto et al. 2018, 2019) As FDU, which affects C and N abundances, only occurs during the ascent onto the RGB, subgiant stars are unaffected by this enrichment.

An alternate approach for this analysis would be to estimate the birth abundances of RGB stars by correcting surface abundance effects from FDU as in Vincenzo et al. (2021). Subgiants are the more attractive option since these observations do not rely on model-dependent corrections. However, RGB stars are more luminous, potentially allowing better coverage of the Galactic disk.

We choose to use Roberts et al. (2023, in prep.) sample as this does not rely on additional layers of modeling, providing a more direct constraint to our model and limiting our systematic uncertainties.

Fig. A1 shows a plot of all APOGEE stars and the Roberts et al. (2023, in prep.)polygon selection criteria. Roberts et al. (2023, in prep.) select a region of stars based on surface gravity $\log g$, and

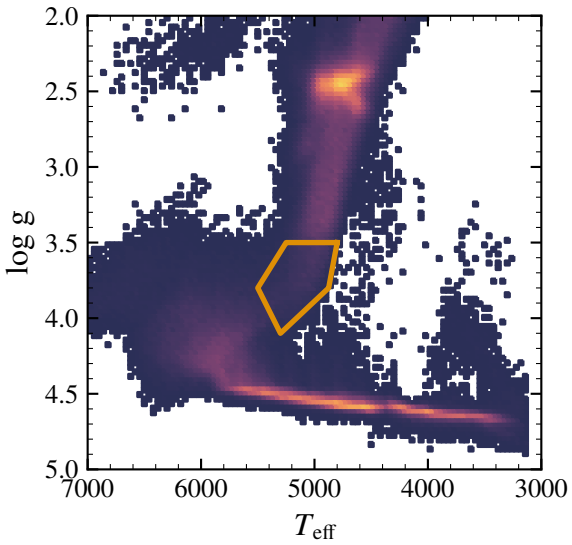

Figure A1. A Kiel diagram of APOGEE stars. Following Roberts et al. (2023, in prep.), we select subgiants in the orange polygon (see Equation A1). These stars have not yet experienced first dredge-up, so their photospheric C and N abundances should reflect their birth mixture.

effective surface temperature, $T_{\rm eff}$.

$$\begin{cases} \log g \geq 3.5 \\ \log g \leq 0.004\,T_{\rm eff} - 15.7 \\ \log g \leq 0.000706\,T_{\rm eff} + 0.36 \\ \log g \leq -0.0015\,T_{\rm eff} + 12.05 \\ \log g \geq 0.0012\,T_{\rm eff} - 2.8. \end{cases} \quad \text{(A1)}$$

Additionally, we included stars in APOGEE marked by the following flags.

- `APOGEE_MIRCLUSTER_STAR`
- `APOGEE_EMISSION_STAR`
- `APOGEE_EMBEDDEDCLUSTER_STAR`
- `young cluster (IN-SYNC)`
- `APOGEE2_W345`
- `EB planet`

This cut isolates a clean sample of ∼12,000 subgiants. We furthermore isolate the low- and high-α sequences with the cut

$$\begin{cases} \text{[Mg/Fe]} > 0.12 - 0.13\,\text{[Fe/H]}, & \text{[Fe/H]} < 0 \\ \text{[Mg/Fe]} > 0.12, & \text{[Fe/H]} > 0. \end{cases} \quad \text{(A2)}$$

The low-α sequence is better reproduced by this model, so we use this cut of the subgiants to compare the models against except for comparing [C/Mg]-[Mg/Fe].

APPENDIX B: AGB YIELD MODELS

A brief summary of the four AGB models we consider, the masses and metallicites of each yield set, and differences between the models.

`C11`. Yields from Cristallo et al. (2011, 2015). Models include masses 1.3, 1.5, 2.0, 2.5, 3.0, 4.0, 5.0, and 6.0 $M_\odot$; and metallicities Z = 0.0001, 0.0003, 0.001, 0.002, 0.003, 0.006, 0.008, 0.01, 0.014, 0.02.

`K10`. Yields are published in Karakas (2010). Models include masses 1.0, 1.25, 1.5, 1.75, 1.9, 2.25, 2.5, 3.0, 3.5, 4.0, 4.5, 5.0, 5.5, 6.0 $M_\odot$; and metallicities Z = 0.0001, 0.004, 0.008, 0.02.

`V13` Yields are published in Ventura et al. (2013, 2014, 2018); Vincenzo et al. (2021), Models include masses 1.5, 2.0, 2.5, 3.0, 3.5, 4.0, 4.5, 5.0, 6.0, 6.5, 7.0 $M_\odot$; and metallicities Z = 0.0003, 0.001, 0.002, 0.004, 0.008, 0.014, 0.04. `V13`is evololved with DHFJKSLDF, `V13`is unusual in that hot bottom burning is much stronger than other models, resulting in much lower stellar yields and negative yields above solar metallicities.

`K16` Yields are published in Karakas & Lugaro (2016); Karakas et al. (2018) Models include masses 1.0, 1.25, 1.5, 1.75, 2.25, 2.5, 2.75, 3.0, 3.25, 3.5, 3.75, 4.0, 4.5, 5.0, 5.5, 6.0, 7.0 $M_\odot$; and metallicities Z = 0.0003, 0.001, 0.002, 0.004, 0.008, 0.014, 0.04. This yield set was extended up to metallicities of 0.1 in DFJSD; however, we do not consider this range here.

This paper has been typeset from a TEX/LATEX file prepared by the author.